Delft University of Technology

Document Version
Final published version

Citation (APA)
Zhao, Y., Peng, Z., Ye, Q., Xu, Y., Yu, H., Chen, L., Wang, Z., & He, Q. (2025). Spatiotemporal variation and generation mechanism of wave nonlinearity across salt marsh vegetation. *Limnology and Oceanography*, *70*(9), 2660-2672. https://doi.org/10.1002/lno.70168

LIMNOLOGY
and
OCEANOGRAPHY

Limnol. Oceanogr. 9999, 2025, 1–13
© 2025 Association for the Sciences of Limnology and Oceanography.
doi: 10.1002/lno.70168

RESEARCH ARTICLE

Spatiotemporal variation and generation mechanism of wave nonlinearity across salt marsh vegetation

Ying Zhao,[1,2,3] Zhong Peng,[1,4*] Qinghua Ye,[2,3] Yuan Xu,[1] Haisheng Yu,[1,2] Liangzhi Chen,[5] Zhengbing Wang,[2,3] Qing He[1]

[1]State Key Laboratory of Estuarine and Coastal Research, East China Normal University, Shanghai, China; [2]Faculty of Civil Engineering and Geosciences, Section of Hydraulic Engineering, Delft University of Technology, Delft, The Netherlands; [3]Deltares, Delft, The Netherlands; [4]Institute of Eco-Chongming, East China Normal University, Shanghai, China; [5]CCCC-Fhdi Engineering Co., Ltd., Guangzhou, China

Abstract

Wave nonlinearity plays a critical role in modulating energy dissipation and sediment transport in vegetated coastal zones, influencing shoreline stability and ecosystem-based defenses. This study analyzes 45 d of wave observations from the Yangtze Estuary, including data collected during Typhoon Khanun, to investigate its spatial variability and underlying mechanisms of wave nonlinearity across a mudflat–vegetation transect. Wave skewness and asymmetry varied within tidal cycles, increasing at low tide and decreasing at high tide. During typhoon conditions, nonlinearity intensified significantly, with skewness increasing by up to 346% and asymmetry shifting toward more forward-leaning waveforms, both closely linked to elevated Ursell numbers. Bispectral analysis at five stations across the transect revealed distinct energy transfer mechanisms: sum interactions dominated over mudflats, whereas difference interactions prevailed within vegetated zones, indicating vegetation-induced modification of nonlinear wave dynamics. Further analysis shows that shoaling and vegetation exerted opposing influences, amplifying and damping wave nonlinearity, respectively. Empirical formulas proposed by Zhao et al. (*Coastal Engineering* 2024; 192:104543) from laboratory data were evaluated against the field data, demonstrating reasonable performance under extreme conditions. These findings improve mechanistic understanding of wave–vegetation interactions and support the development of nature-based strategies for coastal resilience and sediment management.

Coastal salt marsh vegetation plays a crucial role in the stability and functionality of coastal ecosystems, acting as natural buffers that reduce wave energy, protect shorelines, and provide vital habitats needed to sustain biodiversity. The dynamic interaction between waves and salt marsh vegetation has garnered significant attention due to its implications for coastal defense, sediment transport, and ecosystem services. There are plenty of studies on wave-vegetation interactions, covering various aspects such as wave attenuation (Anderson and Smith 2014; He et al. 2019), turbulence generation (Tang et al. 2019; Chen et al. 2020), wave setup reduction (Van Rooijen et al. 2016), and changes in wave spectra (Yang and Irish 2018) and velocity structure (Nepf and Vivoni 2000; Lacy and Wyllie-Echeverria 2011). Despite substantial progress in understanding wave-vegetation interactions, the variation of wave nonlinearity as waves propagate through salt marsh vegetation remains inadequately explored. Incorporating nonlinear processes is essential for predicting wave transformation (Peng et al. 2009; Ma et al. 2017), attenuation (Wu and Cox 2015; Phan et al. 2019), and sediment dynamics (Abreu et al. 2010; Ruessink et al. 2012; Zhao et al. 2024). Moreover, studying wave nonlinearity can contribute to the development of wave propagation models (Chakrabarti et al. 2017).

Numerous studies into wave nonlinearity have employed laboratory experiments to describe the variation of wave nonlinearity as laboratory experiments offer a controlled environment and simplified physical processes. Peng et al. (2009)

---

*Correspondence: zpeng@sklec.ecnu.edu.cn

Deputy editor: Julia Mullarney

Data Availability Statement: The data that support the findings of this study are available from the corresponding author upon reasonable request.

investigated the wave nonlinearity variation over a low-crested breakwater and provided empirical relationships between the skewness (S), asymmetry (A), and local Ursell number (Ur, relative wave height multiplied by relative wavelength squared, $H_s L_m^2/h^3$, where H_s is significant wave height, L_m is the mean wavelength, and h is water depth). Changes in bed slope have been found to affects the relationship between asymmetry, skewness, and Ursell number (Dong et al. 2014; Chen et al. 2023). Rocha et al. (2017) discovered through physical experiments that skewness initially increases from near 0 and then decreases, while asymmetry initially decreases and then increases. In vegetated coastal systems, the interaction becomes even more intricate. Experimental investigations incorporating flexible vegetation have found that S and A are influenced not only by Ur, but also by vegetation properties such as submergence ratio, stem density, and patch width. Zhao et al. (2024) found that wave skewness increases with increasing Ursell number and relative vegetation submergence, but decreases with increasing relative vegetation width and density. Additionally, wave asymmetry increases with increasing relative vegetation submergence, density, and Ursell number, but decreases with increasing relative vegetation width. While laboratory experiments provide valuable insights into wave-vegetation interactions, they are inherently limited by scale effects, and factors such as continuous tidal fluctuations, wave-current interactions, spatial variability in vegetation distribution, and the complex morphology of tidal flats are challenging to replicate under controlled laboratory conditions.

Field observation data effectively reflect real-time hydrodynamic conditions on tidal flats, including the interactions between tidal levels, currents, and wave patterns. Elgar and Guza (1985) found that wave skewness increases from 0 to maximum on natural beaches and decreases by 30%–60% when wave breaking occurs. Wave asymmetry increases from 0 to the maximum and decreases continuously after wave breaking. These findings are similar to the theory developed by Herbers (2003) on a beach with a sand bar: wave skewness increases seaward and decreases shoreward, while asymmetry changes from a negative value seaward to a positive value shoreward. Moreover, similar nonlinear wave variation occurs in natural beaches with rocky platforms (Poate et al. 2018) and coral reef areas (Cheriton et al. 2016). Nevertheless, a clear knowledge gap remains regarding the evolution of wave nonlinearity within field-scale salt marsh vegetation. Salt marshes are characterized by flexible vegetation and highly dynamic hydrodynamic conditions. The interaction between waves and salt marsh vegetation is modulated by multiple co-varying forces, including tidal fluctuations, wave–current coupling, and vegetation properties such as stiffness, stem diameter, density, and height, which collectively influence wave attenuation and energy transfer processes. These dynamic and site-specific features result in complex and time-dependent feedbacks between vegetation motion and wave deformation, which cannot be readily captured by existing models or measurements derived from rigid or static environments such as reefs. Therefore, new in situ measurements are essential to accurately characterize wave transformation processes in salt marshes and to improve parameterizations of wave nonlinearity under such variable and biologically active conditions.

This study focuses on the variation of wave nonlinearity in a spring-neap tidal environment based on field observation data. First, the variations and mechanisms of nonlinearity at the vegetation edge under normal conditions are discussed. Second, the variation of nonlinearity in vegetation during extreme events is analyzed. Finally, the applicability of the laboratory formulae of wave nonlinearity from Zhao et al. (2024) is validated using field data; the differences between field conditions and flume experiments are discussed.

Methodologies

This section provides an overview of the field measurements and the data processing methods.

Field measurements

A 45-day field experiment (28th June to 12th August 2023, all-time series are in China Standard Time, UTC + 8) was conducted at Chongming Island, Shanghai, as depicted in Fig. 1. This region serves as a typical estuarine wetland in the Yangtze River Estuary (Li et al. 2014).

The tidal regime in the Yangtze Estuary is primarily characterized as semi-diurnal, featuring an average tidal cycle of approximately 12 h and 25 min (Zhu et al. 2016). Typically, the average wind speed ranges from 3 to 4 m/s, with the highest wind speeds recorded during the summer storm seasons.

The study positioned five observation points (Fig. 1c) across the salt marsh vegetation from the sea to the land. The measurement instruments used at Offshore, Edge, and Veg2 sites (Table 1) include Nortek Vector Acoustic Doppler Velocimeter (ADV), RBRvirtuoso^3 D|wave 16 (WAVE), and RBRconcerto^3-C.T.D|Tu (TU) (Fig. 1c,d) to measure water levels, waves, currents, and turbidity. In contrast, only the RBRvirtuoso^3 D|wave 16 is deployed at Veg1 and Veg3 for measuring water levels and waves.

The ADV was employed in this study to measure three-dimensional velocity at a position 10 cm above the seabed, corresponding to a sensor head position 25 cm above the bed (there is a blind zone of 15 cm). This configuration was chosen to capture near-bed flow dynamics and sediment transport processes. However, the velocity data were not utilized in this analysis; the sensor's position does not affect the results presented in the study. The sampling interval is set to 5 min, with a sampling frequency of 64 Hz, and the duration is 32 s in burst mode. Wave data are measured by RBR*virtuoso*^{3} D|wave

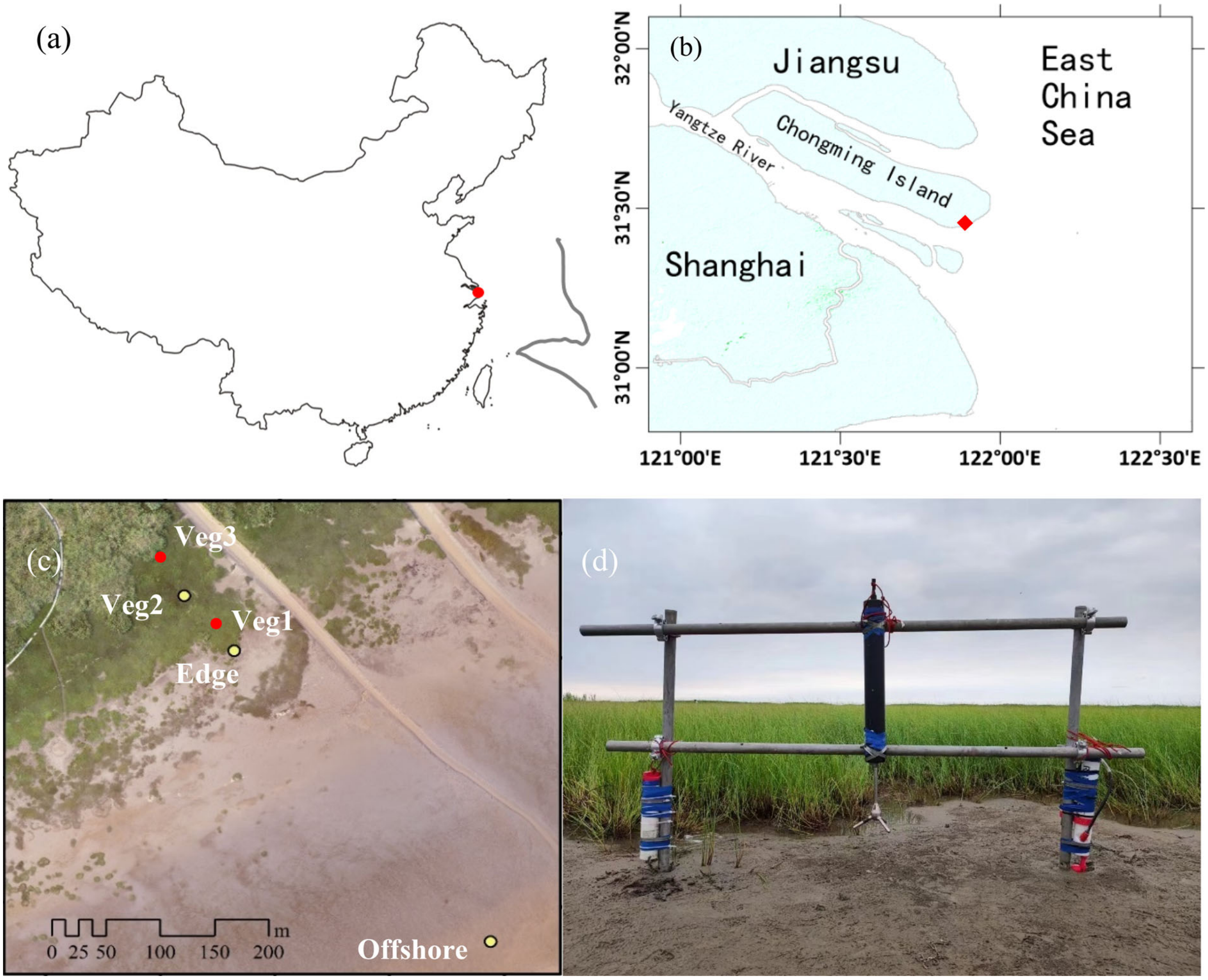

Fig. 1. Overview of the study area and observation points. (**a**) Study area and the tracks of typhoon Khanun (http://typhoon.nmc.cn/web.html). Red dots indicate the field observation locations. (**b**) Overview of the Yangtze River Estuary and Chongming Dongtan. The red square marks the Chongming Dongtan observation area. (**c**) Locations of observation points. (**d**) Photograph of vegetation "Edge" location (121°56′2.5″, 31°27′32.15″N).

16 using pressure sensors, with the sensor positioned 10 cm above the seabed, operating in continuous mode at 16 Hz. Water depth data are obtained using a RBR*concerto*^{3}-C.T.D|Tu, with the sensor positioned 5 cm above the bed, providing a water depth every 5 min. The wind data is downloaded from the Climate Data Store (http://cds.climate.copernicus.eu/#!/home), and the latitude and longitude of the central point are 121.95°E, 31.45°N.

Table 1. Instrument site information.

Location	Relative elevation, *z* (m)	Relative distance (m)	Instrument
Edge	0	0	ADV, RBR*virtuoso*^{3} D|wave 16, RBR*concerto*^{3}-C.T.D|Tu
Veg1	0.44	35	RBR*virtuoso*^{3} D|wave 16
Veg2	0.63	75	ADV, RBR*virtuoso*^{3} D|wave 16, RBR*concerto*^{3}-C.T.D|Tu
Veg3	0.80	120	RBR*virtuoso*^{3} D|wave 16

Vegetation survey

In the research area, the only vegetation species observed along the cross-shore transect shown in Fig. 1 is *Scirpus mariqueter* (Yuan et al. 2014), which can remain upright in water and exhibit swaying movements. During the observation period, we measured vegetation parameters such as density, height, and diameter within the observed area, as depicted in Supporting Information Fig. S1.

Four locations were evenly spaced along the transect between the "Edge" and "Veg3" points shown in Fig. 1. At each location, three 25 × 25 cm quadrats were randomly selected to measure vegetation parameters, including vegetation stems, diameter, and height. In total, 12 quadrats were surveyed;

these data were then extrapolated to estimate stem density, average diameter, and height per square meter.

Data processing

Wave skewness (S), representing the lack of symmetry in the wave profile relative to the horizontal axis, and wave asymmetry (A), indicating the lack of symmetry relative to the vertical axis, have often been used to describe the evolution of wave nonlinearity, as discussed by Elgar and Guza (1985), Peng et al. (2009), Zou and Peng (2011), and Zhao et al. (2024). Here, wave skewness is defined as $S = \frac{\langle (\eta - \overline{\eta})^3 \rangle}{\langle (\eta - \overline{\eta})^2 \rangle^{3/2}}$, and wave asymmetry is defined as $A = \frac{\langle (\eta_h - \overline{\eta_h})^3 \rangle}{\langle (\eta_h - \overline{\eta_h})^2 \rangle^{3/2}}$, where η is the time series of surface elevation, η_h is the Hilbert transform of surface elevation, and $\overline{\eta}$ represents the mean surface elevation (Peng et al. 2009). Positive skewness indicates wave upward, and positive asymmetry denotes wave pitch-backwards. The bispectral analysis is employed to examine wave–wave interactions to understand the variation of wave nonlinearity in the vegetated area. This method helps reveal the degree of phase coupling between different wave frequencies, with the real part of the bispectrum related to wave skewness and the imaginary part to asymmetry (Elgar and Guza 1985). For a detailed explanation of bispectral analysis equations and methodology, please consult the works of Peng et al. (2009) and Zhao et al. (2024).

In this study, the RBR*virtuoso*^{3} D|wave 16 device measured pressure data at a frequency of 16 Hz, subsequently converting them into instantaneous water depths containing wave, tide, and surge information. To isolate wave signals, a filtering approach focusing on the frequency range of 0.003 to 5 Hz, assumed to represent waves, was employed. Spectral analysis was conducted on these wave data to obtain significant wave heights. Wave nonlinearity parameters, including skewness (S) and asymmetry (A), were calculated using high-resolution free surface elevation data sampled at 16 Hz. Each nonlinearity value was computed from a continuous 10-min time series, corresponding to 9600 data points. To ensure data quality and minimize the influence of instrument noise under very low wave energy conditions, only time series with significant wave heights (H_s) greater than 0.02 m were retained for analysis.

Results

During the observation period, the hydrodynamic parameters at the measuring points were affected by Typhoon Khanun. The typhoo's path and the study area are shown in Fig. 1a.

Typhoon Khanun, known as Typhoon Falcon in the Philippines, was a powerful, erratic, and long-lived tropical cyclone in August 2023. Typhoon Khanun (hereafter referred to as typhoon) started as a low-pressure area in the Pacific Ocean. It rapidly intensified into a Category 4-equivalent typhoon (Schauer and Allen 2021) on the Saffir–Simpson scale over the Philippine Sea on 1$^{\text{st}}$ August, before undergoing an eyewall replacement cycle. Although the typhoon did not make landfall in the observation area, its proximity coincided with the astronomic spring tide. The combined effect of these two conditions resulted in a maximum water depth of 1.87 m and a maximum significant wave height of 0.58 m at the Edge location (referred to Fig. 1), which is significantly higher than during the spring tide alone, where the maximum water depth was 1.27 m and the maximum significant wave height was 0.29 m, half of that during the typhoon period.

Figure 2 presents the water depth, significant wave height, and near-bed velocity during the observation period. As shown in Fig. 2, the observation points experienced three complete spring-neap tide cycles. During the latter part of the observation period, the location was subjected to strong hydrodynamic conditions (high water depth, large significant wave height, and high near-bed velocity).

Discussions

Evolution of wave nonlinearity over different tidal cycles

Based on the observational data in Fig. 2, it is evident that while water depth varies according to a pattern (spring-neap tidal), wave height does not exhibit a clear correlation with changes in water depth (i.e., larger water depth does not correspond to larger wave height). Therefore, in this section, four different tidal cycles (tidal cycles in red in Fig. 2) are selected for analysis: large depth-small significant wave height, small depth-small significant wave height, large depth-large wave significant height, and small depth-large significant wave height, as shown in Fig. 3b,c. The corresponding flow velocities are depicted in Fig. 3d, indicating relatively high velocities at shallow depths. The moments of maximum water depth for the four tidal cycles are indicated by dashed lines in Fig. 3. Skewness and asymmetry at these four moments are calculated and shown in Fig. 3a. The results reveal that wave nonlinearity is greater at shallow water depths than at deeper water depths (i.e., the magnitudes of S/A are larger, indicating a higher degree of wave deformation).

Figure 4 presents the bicoherence, the real parts (related to wave skewness), and the imaginary parts (related to wave asymmetry) of the wave bispectrum during four tidal cycles. The results show that at shallow water depths, wave interactions are significantly enhanced at high frequencies (Fig. 4b,d), while at deeper water depths, interactions are more pronounced at low frequencies (Fig. 4a,c). This implies that difference interactions are stronger at deeper water depths, while sum interactions are more prominent at shallow water depths.

There are positive values in both the main frequency and high frequencies of real parts (Fig. 4f,h) at shallow water depths, leading to increased positive skewness. While at

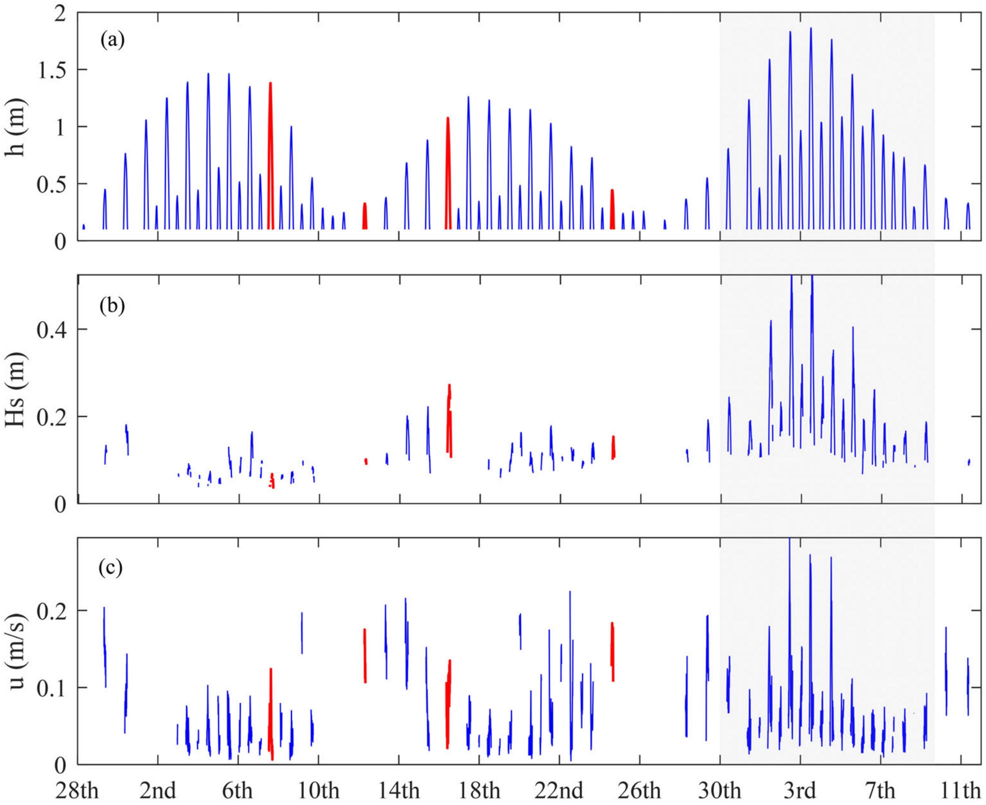

Fig. 2. Time series data at the Edge location: (**a**) water depth, (**b**) significant wave height, and (**c**) near-bed velocity during the measurement period. The shaded portion represents the period affected by the typhoon, while blank sections mark intervals when instruments were not submerged or significant wave heights were below 0.02 m. All time series are in China Standard Time (UTC + 8). Four red tidal cycles are selected to analyze the influence of hydrodynamic parameters on wave nonlinearity.

deeper water depths, negative values occur in the low frequency of real parts (Fig. 4e,g), which offset the positive values at the main frequency, thus reducing skewness. These findings align with the skewness pattern shown in Fig. 3a. The imaginary parts of the bispectrum at the main frequency and high frequencies are negative at shallow water depths, resulting in overall negative asymmetry (Fig. 4j,l). Conversely, at deeper water depths, positive values at low frequencies counterbalance the negative values at the main frequency, resulting in positive (Fig. 4i) or near-zero asymmetry (Fig. 4k). The bispectral results are consistent with the asymmetry variation pattern shown in Fig. 3a.

In conclusion, despite differing hydrodynamic conditions across the four tidal cycles, the correlation between nonlinearity and water depth remains strong. Nonlinearity is greater at shallow water depths due to significant wave–wave interaction at high frequency, where the real/imaginary parts at high frequencies and the main frequency positively reinforce each other. At deeper water depths, significant wave–wave interaction at low frequency results in real/imaginary parts at low and main frequencies counteracting each other, leading to weaker nonlinearity.

Typhoon impact on wave nonlinearity

Figure 5a–h illustrates the relationships between wave nonlinearity indicators—skewness (*S*) and asymmetry (*A*)—and hydrodynamic parameters including water depth (*h*), significant wave height (H_s), mean wave period (T_m), and the Ursell number (*Ur*) under both normal and storm conditions at the Edge location.

Under normal conditions, skewness generally decreases with increasing water depth, while it increases with significant wave height, mean period, and the Ursell number, showing positive correlations. In contrast, asymmetry tends to become more negative (indicating greater forward-leaning waveforms) as wave height and mean period increase, with storm conditions producing significantly more negative values than under normal conditions. Furthermore, both skewness and asymmetry exhibit strong correlations with the Ursell number, suggesting that nonlinear wave behavior intensifies with increasing nonlinearity index.

Figure 5i–p presents the relationships between wave nonlinearity indicators—skewness (*S*) and asymmetry (*A*)—and hydrodynamic parameters, including water depth (*h*), significant wave height (H_s), mean wave period (T_m), and the Ursell

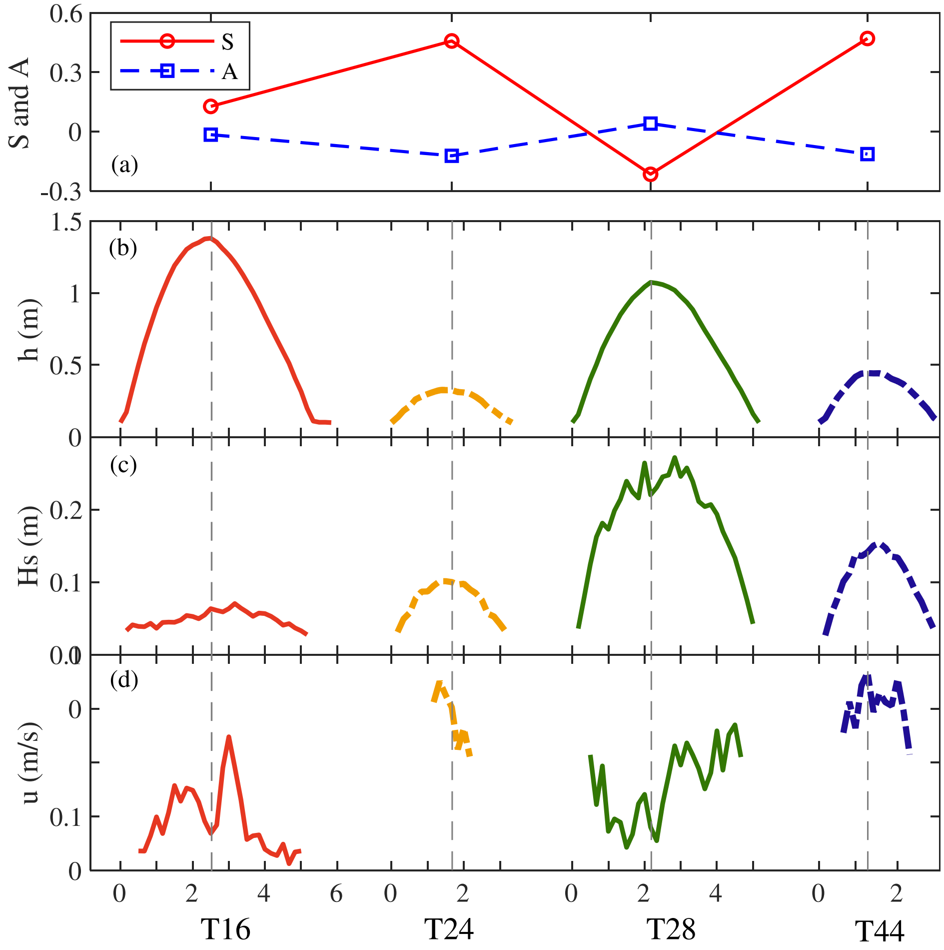

Fig. 3. (**a**) Skewness and asymmetry at different hydrodynamic conditions; variation of (**b**) water depth, (**c**) significant wave height, and (**d**) near-bed velocity at the Edge location. T16, T24, T28, and T44 represent four tidal cycles marked in red in Fig. 2.

number (*Ur*) at the Veg2 location, under both normal and storm conditions.

Under normal conditions, skewness exhibits a decreasing trend with increasing water depth, while it shows a positive correlation with significant wave height, mean wave period, and the Ursell number. In contrast, asymmetry tends to become more negative with increasing *Ur* and mean period, whereas its relationship with water depth and wave height is less pronounced. During storm conditions, the magnitudes of skewness and asymmetry are positively correlated with *Ur*; but the relationship with other hydrodynamic parameters is weakened.

The Yangtze River Estuary, situated along the Pacific coast, is frequently influenced by storms, particularly from July to September. On average, 2–3 storms affect the estuary and its adjacent waters annually, with some years experiencing up to 5–6 events (Ding and Ge 2013). In addition to examining wave nonlinearity under normal conditions, it is crucial to investigate how extreme weather events, such as typhoons, modulate wave nonlinearity in the intertidal zone. During typhoons, intensified hydrodynamic forces often lead to increased wave nonlinearity. Therefore, understanding wave nonlinearity in vegetated areas under extreme conditions, such as during typhoons, is crucial for improving our knowledge of these complex processes.

Figure 5a–h illustrates that wave nonlinearity is markedly enhanced during storm events. The average skewness increases from 0.13 under normal conditions to 0.58 during storms, representing a 346% increase. The maximum skewness rises from 0.64 to 0.97, with standard deviations of 0.21 and 0.16, respectively. Similarly, the magnitude of asymmetry increases sharply, with mean values shifting from −0.023 to −0.15. The peak asymmetry changes from −0.27 to −0.33, and the standard deviations are 0.078 and 0.11, respectively. Figure 5i–p presents a similar pattern at the Veg2 location: average skewness increases from 0.29 to 1.17, representing a fourfold increase during storms. The maximum skewness slightly increases from 1.57 to 1.63, with standard deviations of 0.35 and 0.17. Likewise, asymmetry shifts from 0.0074 to −0.28, and the peak values change from −0.35 to −0.61, with

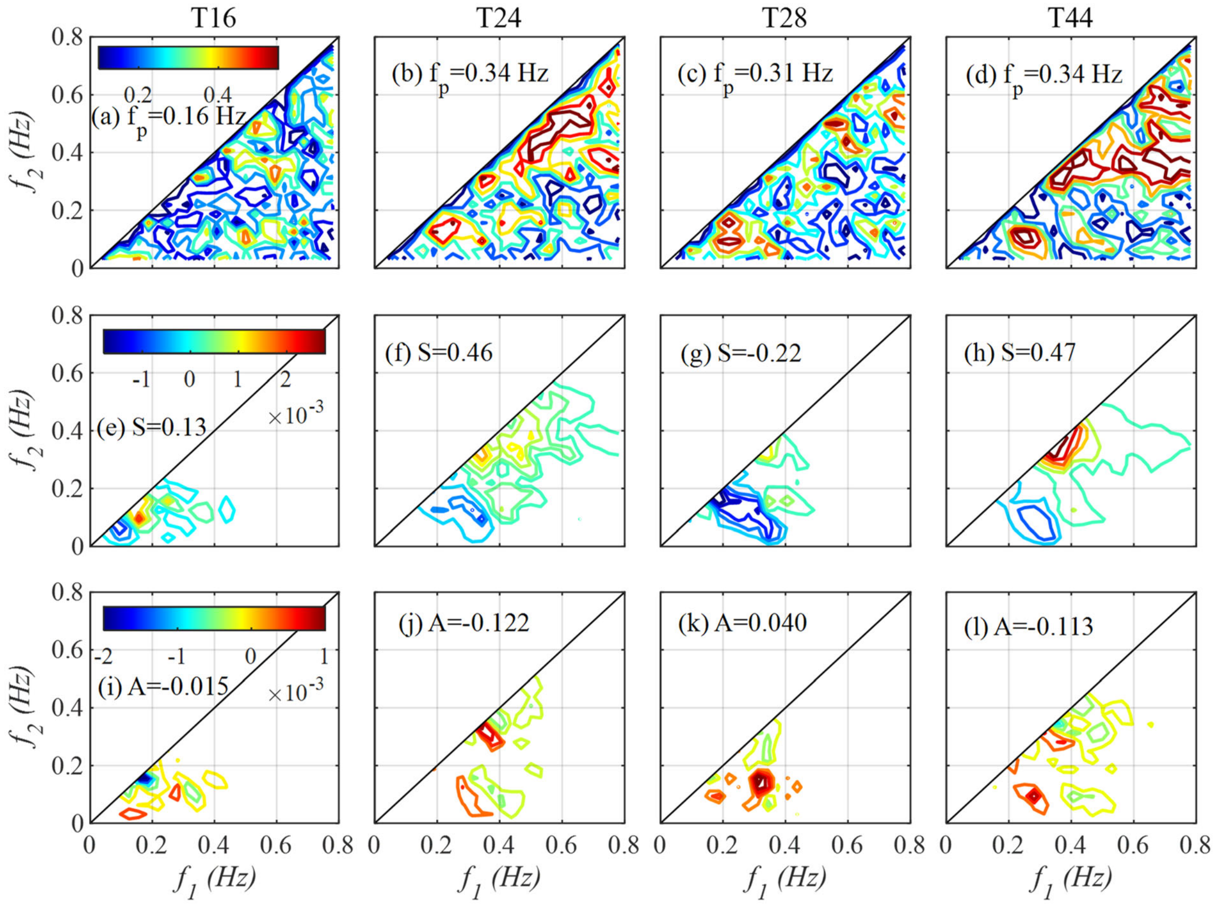

Fig. 4. Bispectrum of surface elevations at the Edge location. (**a–d**) the bicoherence, b(f_1, f_2), (**e–h**) the real part of bispectrum, $\Re\{Bs(f_1, f_2)\}$, and (**i–l**) the imaginary part of bispectrum, $\Im\{Bs(f_1, f_2)\}$. T16 and T28 represent spring tidal cycles, while T24 and T44 represent neap tidal cycles.

standard deviations of 0.096 and 0.14. These results indicate a pronounced enhancement of forward-pitched waveforms under storm conditions.

Figure 5 illustrates that skewness increases with rising *Ur* (more peaked waves), while the magnitudes of asymmetry increase as *Ur* increases (more pitch-forward waves), consistent with patterns observed on the incident side of smooth low-crested breakwaters (Peng et al. 2009; Zou and Peng 2011). Moreover, Fig. 5 shows that the relationship between the Ursell number and both skewness and asymmetry is not influenced by the presence of typhoons, indicating that the same patterns persist under both normal and typhoon conditions. Figure 5l shows that wave skewness (*S*) increases almost linearly with the Ursell number (*Ur*) under normal conditions, with a clear upward trend. During storm conditions, skewness still increases with *Ur*; however, the increasing rate decreases.

Different mechanisms of wave nonlinearity generation with and without vegetation

Although it is well established that nonlinearities, including harmonic generation, commonly emerge as waves propagate into shallow waters, the specific mechanisms by which vegetation modulates these nonlinear wave characteristics remain insufficiently explored. Compared to mudflats, vegetated shallow environments introduce additional complexity due to vegetation-induced drag, flexibility, and spatial heterogeneity. These factors may fundamentally alter the generation and evolution of wave skewness and asymmetry. Therefore, it is essential to investigate different mechanisms of wave nonlinearity generation with and without vegetation.

Bispectral analysis reveals distinct mechanisms responsible for the generation of wave nonlinearity with and without vegetation. For the amplitude of the bispectrum (Fig. 6a–e), the transition from Offshore (Fig. 6a) to Edge (Fig. 6b) demonstrates enhanced energy at both main and high frequencies, indicating intensified sum interaction due to shoaling effects over the mudflat. This pattern is consistent with previous findings (Elgar and Guza 1985) and Fig. 4. In contrast, nonlinear variations within the vegetated zone are driven by energy changes and transfers among low- and high-frequency pairs, influenced by vegetation. Due to the effects of vegetation width and wavelength, the interaction between vegetation and short waves within the wave group becomes more pronounced. This leads to a weakening of high-frequency

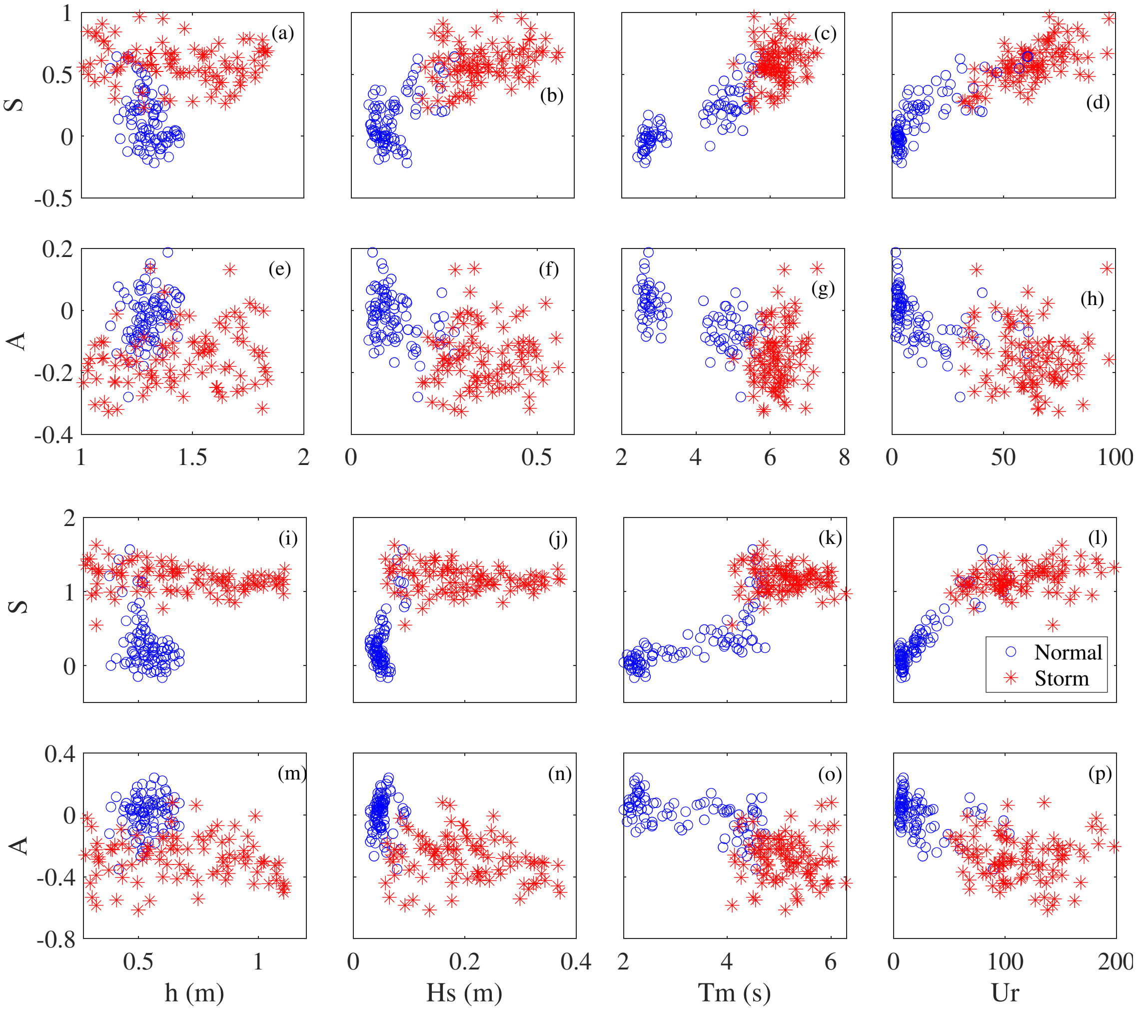

Fig. 5. Relationship between water depth (*h*), significant wave height (H_s), wave period (T_m), Ursell number (*Ur*) and skewness (*S*) and asymmetry (***A***) at (**a–h**) Edge location (Fig. 1) and (**i–p**) Veg2 location (Fig. 1).

coupling (i.e., reduced sum interaction) while enhancing low-frequency coupling (strengthened difference interaction) (Fig. 6b–e), demonstrating a distinct wave nonlinearity generation mechanism compared to mudflats. A similar pattern is observed in the spatial evolution of phase (Fig. 6a–e), confirming the different underlying mechanisms. Furthermore, the phase analysis (Fig. 6f–j) indicates that the lower-frequency wave component is bound to the incident waves, with a phase difference of approximately 180° (around −90° at main frequency in Fig. 6g, and about 90° at low-frequency in Fig. 6j).

Variations of wave nonlinearity across the vegetation

Vegetation is an important component of the intertidal zone. In our study, under normal conditions, the inundation period in the vegetated area is short and hydrodynamic forces are weak, making the investigation of wave nonlinearity less meaningful.

Figure 7a,b shows the spatial variation of wave skewness and asymmetry across the mudflat and vegetated zone. As waves propagate landward, wave skewness increases from the offshore mudflat toward the front of the vegetated region, reaching a peak at Veg2 before slightly decreasing toward Veg3. Wave asymmetry also increases in magnitude along the vegetated transect, becoming most pronounced at Veg2, and then slightly declining at the rear end of the vegetation. This pattern suggests that vegetation exerts a location-dependent modulation on nonlinear wave characteristics.

The red lines in Fig. 7a,b illustrate the variation of wave skewness and asymmetry during the maximum water depth period during one tidal cycle across five observation points. Wave skewness increases steadily from the mudflat (Offshore) to the front part of the vegetated area (Veg2), with a slight decrease from Veg2 to Veg3, but remains significantly higher than the initial value. Wave asymmetry shifts from positive to negative over the mudflat, with increasing magnitude. Upon

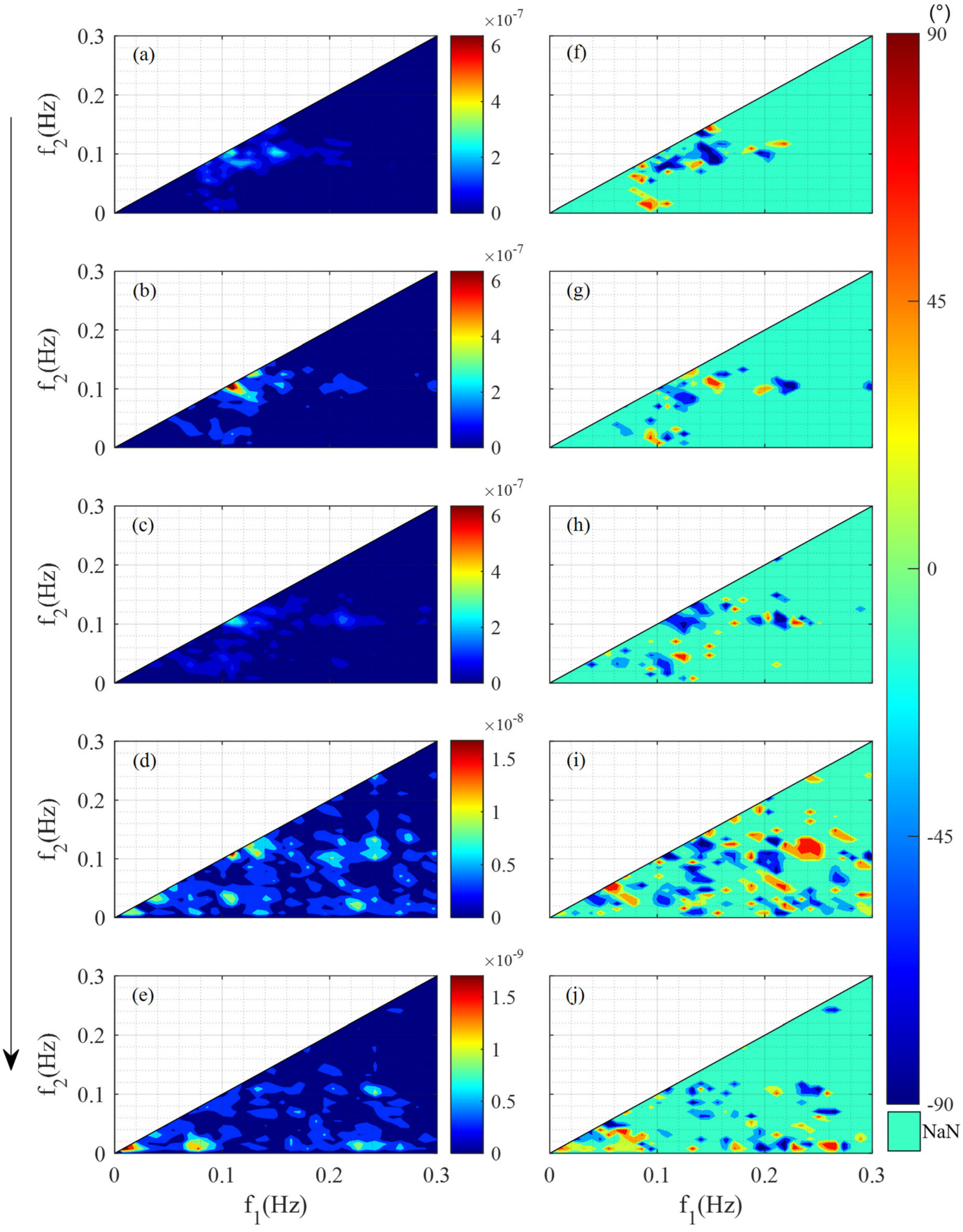

Fig. 6. Bispectral analysis at five observation points. (**a–e**) the amplitude of bispectrum; (**f–j**) the phase of bispectrum, arctan($\Re\{Bs(f_1, f_2)\}/\Im\{Bs(f_1, f_2)\}$). The arrow direction indicates the cross-shore transect from offshore mudflat to saltmarsh. In regions where the amplitude is low (indicated by deep blue), the signal-to-noise ratio is too low to yield reliable phase information, and the corresponding phase values are excluded (NaN).

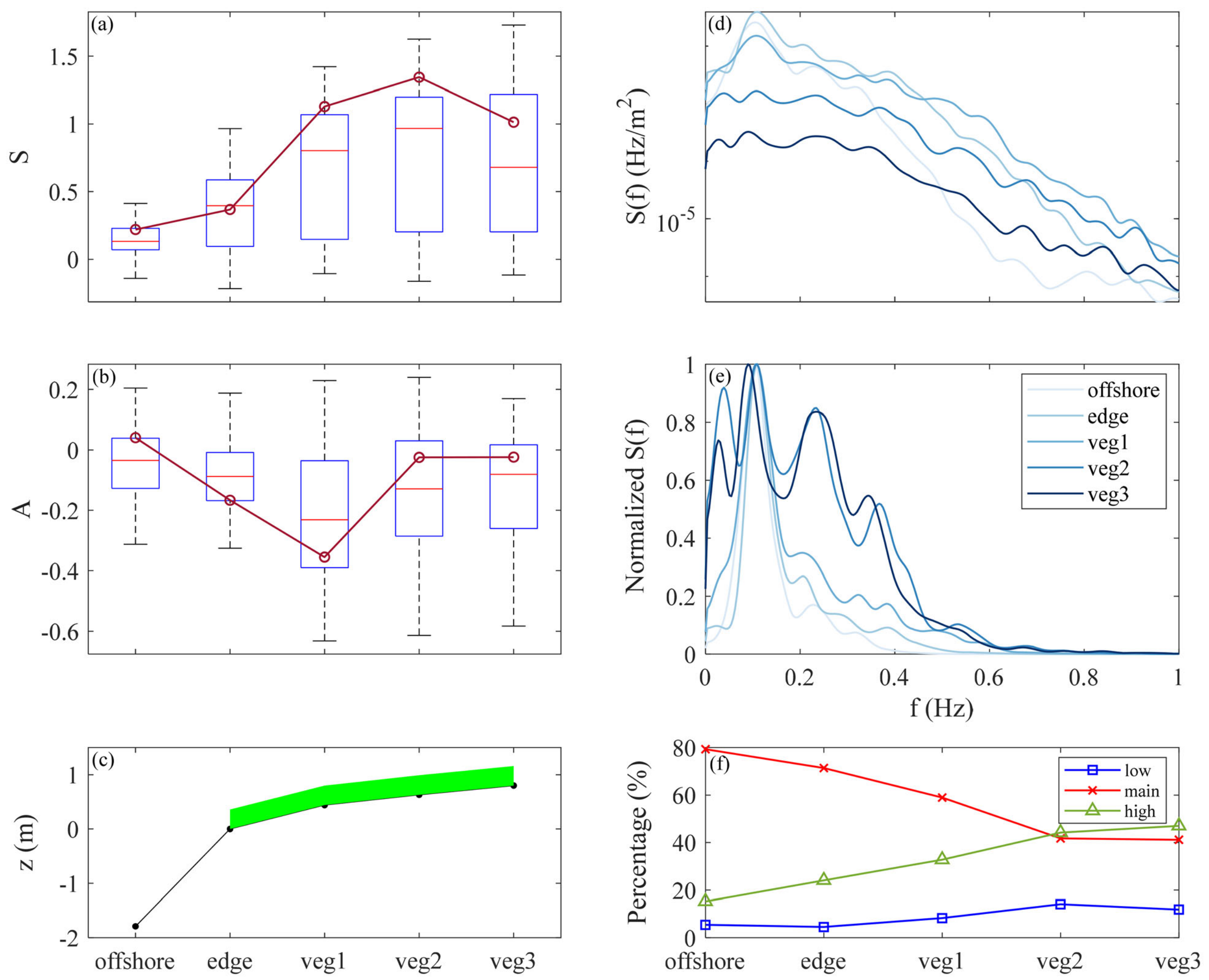

Fig. 7. Changes in (**a**) skewness and (**b**) asymmetry during the tidal flat. The red lines represent the variation of wave skewness and asymmetry during the maximum water depth period during one tidal cycle. (**c**) Relative bed elevations at the observation points (as detailed in Table 1). This figure is not to scale; the green patch is a schematic representation of salt marsh vegetation. (**d**) Wave spectra; (**e**) normalized wave spectra; (**f**) proportion of energy in the low-, peak-, and high-frequency bands relative to the total energy during the maximum water depth period.

entering the vegetated region (from Edge to Veg1), the magnitude of asymmetry further increases, followed by a reduction between Veg1 and Veg3.

Figure 7d presents the power spectra at the five locations, with a dominant peak at approximately 0.11 Hz. Wave energy slightly increases from Offshore to Edge due to shoaling effects on the mudflat but decreases rapidly upon entering the vegetated area (from Edge to Veg3). To highlight the relative energy distribution, spectra were normalized by their maximum values ($S(f)/S(f)_{\max}$), as shown in Fig. 7e. The results indicate a gradual increase in both low- and high-frequency energy proportions during wave propagation, with the most prominent changes observed at Veg2 and Veg3. To quantify this evolution, the spectral energy is divided into three frequency bands: low-frequency (0–0.5f_p), main-frequency (0.5f_p–2f_p), and high-frequency (2f_p–8 Hz). The corresponding energy proportions are shown in Fig. 7f. The results reveal a consistent decrease in main-frequency energy and a pronounced increase in high-frequency energy, while low-frequency energy generally increases but slightly declines at the rear of the vegetated zone.

By integrating Figs. 4, 6, and 7, the mechanisms underlying the variation of wave skewness and asymmetry within the vegetated region can be further clarified. Moreover, the difference between nonlinearities induced by decreasing water depth and those caused by vegetation can be elucidated. Fig. 6 shows that vegetation suppresses sum interactions while promoting difference interactions between wave components, which ultimately leads to a reduction in wave nonlinearity. In contrast, Fig. 4 reveals that a decrease in water depth tends to enhance sum interactions and suppress difference interactions, thereby amplifying wave nonlinearity. These findings suggest that vegetation and depth exert opposing influences on wave–wave interactions and the development of nonlinearity.

Along the observational transect (from Edge to Veg3), wave propagation is simultaneously affected by variations in water depth and the presence of vegetation. In the front section of the vegetated zone (Edge to Veg1), the influence of vegetation is minimal, allowing water depth to dominate the evolution of wave nonlinearity, which results in a rapid increase in skewness and asymmetry. Further along the transect, in the rear part of the vegetated zone (Veg2 to Veg3), vegetation-induced damping becomes more prominent, gradually reducing wave nonlinearity. Overall, as waves propagate through the vegetated region, the relative influence of water depth weakens while the vegetation effect strengthens, with a balance achieved in the middle of the vegetated zone. This interpretation is consistent with the results shown in Fig. 7.

Application of wave nonlinearity formula by Zhao et al. (2024)

In prior research, empirical formulas for wave skewness and asymmetry are frequently derived based on the Ursell number in scenarios without vegetation (Doering and Bowen 1995; Zou and Peng 2011; Ma et al. 2017). Recently, Zhao et al. (2024) found that vegetation characteristics significantly influence wave nonlinearity based on data from two sets of flume experiments. They observed that wave skewness increases with increasing Ursell number and relative vegetation submergence, but decreases with increasing relative vegetation width and density. Additionally, wave asymmetry increases with increasing relative vegetation submergence, density, and Ursell number, but decreases with increasing relative vegetation width. Building on these findings, they proposed a modified Ursell number, Ur_{veg}, and further fitted empirical formulas for wave skewness and asymmetry within vegetation. To validate the applicability of their formulas and conclusions using field observation data, we plotted the relationship between Ur_{veg} and measured skewness and asymmetry, as shown in Fig. 8, including data during normal conditions and typhoon events. The black lines in the graph represent the empirical formulas proposed by Zhao et al. (2024).

Figure 8 illustrates that, under typhoon conditions, the empirical formulas by Zhao et al. (2024) perform reasonably well in capturing the observed trends in wave skewness and asymmetry. Most of the storm-event data points cluster around the fitted lines, suggesting that the formulas are effective in characterizing enhanced nonlinearity during extreme hydrodynamic forcing. However, under normal conditions, the formulas tend to slightly overestimate wave asymmetry in the Ur_{veg} range of 0.9 to 1.5. This discrepancy may arise from differences in vegetation type and field variability. First, *Spartina alterniflora* is used in the flume test, while the actual field observation involves a more flexible type of vegetation, *S. mariqueter*. The difference in the forces exerted by the vegetation roots and leaves on the waves is greater, with a significantly greater obstruction to wave troughs than wave crests, leading to increased forward tilting of the waves. The discrepancies in results can also be attributed to the combined effects of multiple hydrodynamic drivers—such as waves, currents, and winds—in natural field conditions, as well as variations in the ranges of vegetation parameters employed across different studies. Second, the dispersion of data points can be attributed to the rapid changes in water depth during tidal environments. While the water depth between adjacent data points can vary significantly due to

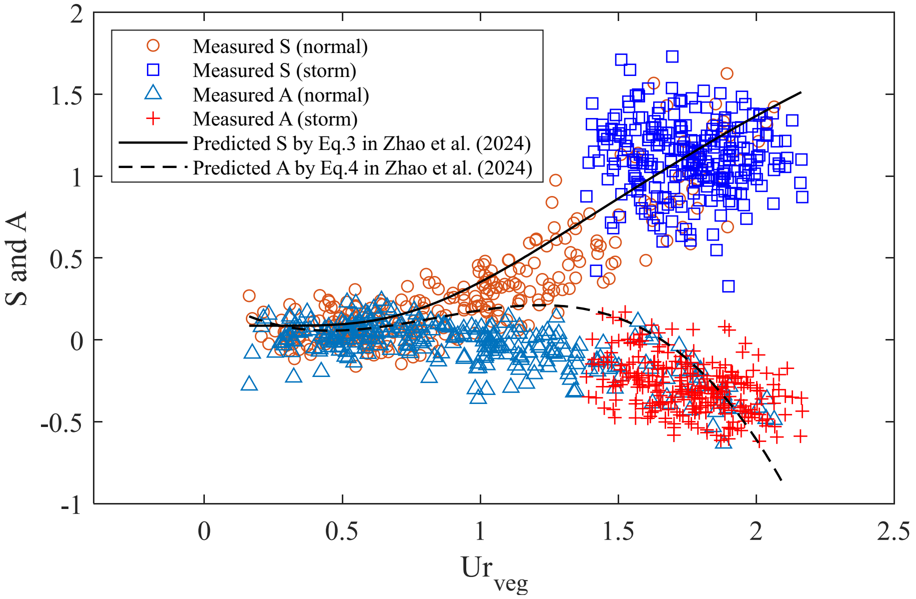

Fig. 8. Relationship between Ur_{veg} and measured skewness and asymmetry, with black lines representing the empirical formulas proposed by Zhao et al. (2024).

rapid ebb and flood tides, the wave height and wavelength tend to change more gradually, resulting in substantial variations in the Ursell number.

This application significantly enhances the practical utility of the wave nonlinearity formulae proposed by Zhao et al. (2024) by transitioning from controlled laboratory conditions to complex, real-world environments. The validation through comprehensive field observations, including data collected during extreme events like Typhoon Khanun, suggests the formulas are effective in characterizing enhanced nonlinearity during extreme hydrodynamic forcing.

This study investigates the variation of wave nonlinearity under a tidal environment using field measurement data collected in the Yangtze Estuary. Spectral and bispectral analyses are used to examine the mechanism of wave nonlinearity in the tidal flats. Results reveal that nonlinearity is greater at shallow water depths due to stronger high-frequency interactions, where the real/imaginary parts at high frequencies and the main frequency positively reinforce each other. At higher water depths, stronger low-frequency interactions result in real/imaginary parts at low and main frequencies counteracting each other, leading to weaker nonlinearity. Wave nonlinearity is higher during a typhoon event than under normal conditions, with an increased upward and forward. Wave skewness gradually increases and remains positive as the waves propagate through the vegetation area. Wave asymmetry decreases along the vegetation, reaching its minimum within vegetation, followed by a slight increase. Vegetation suppresses sum interaction while amplifying difference interaction, revealing a distinct wave nonlinearity generation mechanism compared to mudflats. Within salt marshes, vegetation and wave shoaling exert opposing effects on wave nonlinearity. Meanwhile, the validation of empirical formulas extent confirms their accuracy and provides insights into the factors contributing to errors. The findings of this study improve our understanding of the spatiotemporal variation of wave nonlinearity in the intertidal zone and provide a tool for engineers to quickly calculate wave nonlinearity over salt marsh vegetation.

Author Contributions

Ying Zhao: Writing—original draft, Methodology, Investigation, Formal analysis, Data curation. Zhong Peng: Writing—review and editing, validation, supervision, methodology, funding acquisition, data curation, conceptualization. Qinghua Ye: Writing—review and editing, Methodology. Yuan Xu: Methodology, Data curation. Haisheng Yu: Writing—review and editing, Methodology, Data curation. Liangzhi Chen: Methodology, Funding acquisition. Zhengbing Wang: Writing—review and editing, validation, methodology. Qing He: Writing—review and editing, funding acquisition.

Acknowledgments

The authors thank Anna M. Crawford for generously supplying her bispectrum code for the present work. The authors are also grateful to Xianjin Chen, Dan Fang, Ke Deng, Zhiyang Zhu, Changyang Li, Xi Lu, and Chen Chen for their assistance in the fieldwork. The authors acknowledge the support of the National Key Research and Development Program of China, China (Grant 2022YFE0136700 and 2022YFA1004401) and the Science and Technology Commission of Shanghai Municipality, China (Grant 23002400400, 22JC1400900, and 21230750600). National Natural Science Foundation of China, China (Grant U2040216) is also acknowledged.

Conflicts of Interest

None declared.

References

Abreu, T., P. A. Silva, F. Sancho, and A. Temperville. 2010. “Analytical Approximate Wave Form for Asymmetric Waves.” *Coastal Engineering* 57: 656–667. https://doi.org/10.1016/j.coastaleng.2010.02.005.

Anderson, M. E., and J. M. Smith. 2014. “Wave Attenuation by Flexible, Idealized Salt Marsh Vegetation.” *Coastal Engineering* 83: 82–92. https://doi.org/10.1016/j.coastaleng.2013.10.004.

Chakrabarti, A., S. R. Brandt, Q. Chen, and F. Shi. 2017. “Boussinesq Modeling of Wave-Induced Hydrodynamics in Coastal Wetlands.” *Journal of Geophysical Research: Oceans* 122: 3861–3883. https://doi.org/10.1002/2016JC012093.

Chen, M., S. Lou, S. Liu, et al. 2020. “Velocity and Turbulence Affected by Submerged Rigid Vegetation under Waves, Currents and Combined Wave–Current Flows.” *Coastal Engineering* 159: 103727. https://doi.org/10.1016/j.coastaleng.2020.103727.

Chen, S., Y. Li, C. Zhang, H. Zhu, Q. Li, and J. Shi. 2023. “Effects of Currents on Nonlinear Wave Transformation in a Reef-Lagoon-Channel System.” *Ocean Engineering* 281: 114640. https://doi.org/10.1016/j.oceaneng.2023.114640.

Cheriton, O. M., C. D. Storlazzi, and K. J. Rosenberger. 2016. “Observations of Wave Transformation Over a Fringing Coral Reef and the Importance of Low-Frequency Waves and Offshore Water Levels to Runup, Overwash, and Coastal Flooding.” *Journal of Geophysical Research: Oceans* 121: 3121–3140. https://doi.org/10.1002/2015JC011231.

Ding, P., and J. Ge. 2013. “Analysis of Disastrous Weather in the Hengsha Shoaland Adjacent Waters of the Yangtze Estuary.” *Journal of East China Normal University (Natural Science)* 04: 83–89. https://doi.org/10.3969/j.issn.1000-5641.2013.04.007.

Doering, J. C., and A. J. Bowen. 1995. “Parametrization of Orbital Velocity Asymmetries of Shoaling and Breaking Waves Using Bispectral Analysis.” *Coastal Engineering* 26: 15–33. https://doi.org/10.1016/0378-3839(95)00007-X.

Dong, G., H. Chen, and Y. Ma. 2014. "Parameterization of Nonlinear Shallow Water Waves Over Sloping Bottoms." *Coastal Engineering* 94: 23–32. https://doi.org/10.1016/j.coastaleng.2014.08.012.

Elgar, S., and R. T. Guza. 1985. "Observations of Bispectra of Shoaling Surface Gravity Waves." *Journal of Fluid Mechanics* 161: 425–448. https://doi.org/10.1017/S0022112085003007.

He, F., J. Chen, and C. Jiang. 2019. "Surface Wave Attenuation by Vegetation With the Stem, Root and Canopy." *Coastal Engineering* 152: 103509. https://doi.org/10.1016/j.coastaleng.2019.103509.

Herbers, T. H. C. 2003. "Shoaling Transformation of Wave Frequency-Directional Spectra." *Journal of Geophysical Research* 108: 3013. https://doi.org/10.1029/2001JC001304.

Lacy, J. R., and S. Wyllie-Echeverria. 2011. "The Influence of Current Speed and Vegetation Density on Flow Structure in Two Macrotidal Eelgrass Canopies: A Field Study of Eelgrass Hydrodynamics." *Limnology and Oceanography: Fluids and Environments* 1: 38–55. https://doi.org/10.1215/21573698-1152489.

Li, X., Y. Zhou, L. Zhang, and R. Kuang. 2014. "Shoreline Change of Chongming Dongtan and Response to River Sediment Load: A Remote Sensing Assessment." *Journal of Hydrology* 511: 432–442. https://doi.org/10.1016/j.jhydrol.2014.02.013.

Ma, Y., H. Chen, X. Ma, and G. Dong. 2017. "A Numerical Investigation on Nonlinear Transformation of Obliquely Incident Random Waves on Plane Sloping Bottoms." *Coastal Engineering* 130: 65–84. https://doi.org/10.1016/j.coastaleng.2017.10.003.

Nepf, H. M., and E. R. Vivoni. 2000. "Flow Structure in Depth-Limited, Vegetated Flow." *Journal of Geophysical Research: Oceans* 105: 28547–28557. https://doi.org/10.1029/2000JC900145.

Peng, Z., Q. Zou, D. Reeve, and B. Wang. 2009. "Parameterisation and Transformation of Wave Asymmetries over a Low-Crested Breakwater." *Coastal Engineering* 56: 1123–1132. https://doi.org/10.1016/j.coastaleng.2009.08.005.

Phan, K. L., M. J. F. Stive, M. Zijlema, H. S. Truong, and S. G. J. Aarninkof. 2019. "The Effects of Wave Non-Linearity on Wave Attenuation by Vegetation." *Coastal Engineering* 147: 63–74. https://doi.org/10.1016/j.coastaleng.2019.01.004.

Poate, T., G. Masselink, M. J. Austin, M. Dickson, and R. McCall. 2018. "The Role of Bed Roughness in Wave Transformation Across Sloping Rock Shore Platforms: Bed Roughness on Wave Transformation." *Journal of Geophysical Research. Earth Surface* 123: 97–123. https://doi.org/10.1002/2017JF004277.

Rocha, M. V. L., H. Michallet, and P. A. Silva. 2017. "Improving the Parameterization of Wave Nonlinearities—The Importance of Wave Steepness, Spectral Bandwidth and Beach Slope." *Coastal Engineering* 121: 77–89. https://doi.org/10.1016/j.coastaleng.2016.11.012.

Ruessink, B. G., G. Ramaekers, and L. C. van Rijn. 2012. "On the Parameterization of the Free-Stream Non-Linear Wave Orbital Motion in Nearshore Morphodynamic Models." *Coastal Engineering* 65: 56–63. https://doi.org/10.1016/j.coastaleng.2012.03.006.

Schauer, J., and A. Allen. 2021. *Tropical Cyclone Names and Definitions*. National Weather Service. https://doi.org/10.55460/581V-SWP2.

Tang, C., J. Lei, and H. M. Nepf. 2019. "Impact of Vegetation-Generated Turbulence on the Critical, Near-Bed, Wave-Velocity for Sediment Resuspension." *Water Resources Research* 55: 5904–5917. https://doi.org/10.1029/2018WR024335.

Van Rooijen, A. A., R. T. McCall, J. S. M. Van Thiel De Vries, A. R. Van Dongeren, A. J. H. M. Reniers, and J. A. Roelvink. 2016. "Modeling the Effect of Wave-Vegetation Interaction on Wave Setup." *Journal of Geophysical Research: Oceans* 121: 4341–4359. https://doi.org/10.1002/2015JC011392.

Wu, W.-C., and D. T. Cox. 2015. "Effects of Wave Steepness and Relative Water Depth on Wave Attenuation by Emergent Vegetation." *Estuarine, Coastal and Shelf Science* 164: 443–450. https://doi.org/10.1016/j.ecss.2015.08.009.

Yang, Y., and J. L. Irish. 2018. "Evolution of Wave Spectra in Mound-Channel Wetland Systems." *Estuarine, Coastal and Shelf Science* 207: 444–456. https://doi.org/10.1016/j.ecss.2017.06.012.

Yuan, L., Z. Ge, X. Fan, and L. Zhang. 2014. "Ecosystem-Based Coastal Zone Management: A Comprehensive Assessment of Coastal Ecosystems in the Yangtze Estuary Coastal Zone." *Ocean and Coastal Management* 95: 63–71. https://doi.org/10.1016/j.ocecoaman.2014.04.005.

Zhao, Y., Z. Peng, X. Chen, et al. 2024. "Parameterisation and Evolution of Non-Breaking Wave Nonlinearity Over Flexible Vegetation." *Coastal Engineering* 192: 104543. https://doi.org/10.1016/j.coastaleng.2024.104543.

Zhu, Q., B. C. van Prooijen, Z. B. Wang, Y. X. Ma, and S. L. Yang. 2016. "Bed Shear Stress Estimation on an Open Intertidal Flat Using In Situ Measurements." *Estuarine, Coastal and Shelf Science* 182: 190–201. https://doi.org/10.1016/j.ecss.2016.08.028.

Zou, Q., and Z. Peng. 2011. "Evolution of Wave Shape Over a Low-Crested Structure." *Coastal Engineering* 58: 478–488. https://doi.org/10.1016/j.coastaleng.2011.01.001.

Supporting Information

Additional Supporting Information may be found in the online version of this article.

Submitted 14 November 2024
Revised 06 June 2025
Accepted 29 July 2025